Pharm Res (2014) 31:2762–2773
DOI 10.1007/s11095-014-1373-8

RESEARCH PAPER

Infrared Spectroscopic Imaging Tracks Lateral Distribution in Human Stratum Corneum

Qihong Zhang • Peter Saad • Guangru Mao • Russel M. Walters • Mary Catherine Mack Correa • Richard Mendelsohn • Carol R. Flach

Received: 14 January 2014 / Accepted: 21 March 2014 / Published online: 3 May 2014
© Springer Science+Business Media New York 2014

ABSTRACT

Purpose To demonstrate the efficacy of infrared (IR) spectroscopic imaging for evaluation of lateral diffusion in stratum corneum (SC) and for elucidation of intermolecular interactions between exogenous agents and SC constituents.

Methods In separate experiments, acyl chain perdeuterated oleic acid (OA-d) and deuterated dimethyl sulfoxide (DMSO-d) were applied to the surface of isolated human SC. The lateral distribution of permeant concentrations was monitored using the time-dependence of IR images. Diffusion coefficients (D) were estimated from Fick's second law. Interactions between the exogenous agents and the SC were tracked from changes in CD_2 and Amide I stretching frequencies.

Results Networked glyphs served as the major pathway for lateral distribution of OA-d. In glyph-poor regions, D values from $0.3–1 \times 10^{-8}$ cm^2/s bracketed the OA-d data and apparently decreased with time. Although diffusion of DMSO-d is relatively fast compared to our experimental measurement time, the results suggest values of $\sim 10^{-7}$ cm^2/s. OA-d spectral changes suggest penetration into the ordered lipids of the SC; DMSO-d penetration results in perturbation of SC keratin structure.

Conclusions IR imaging provides concentration profiles, diffusion coefficients, and unique molecular level information about structural changes in the endogenous SC constituents and exogenous agents upon their mutual interaction. Transport along glyphs is the dominant mode of distribution for OA-d.

KEY WORDS glyphs · Infrared (IR) imaging · lateral diffusion · stratum corneum

Q. Zhang • P. Saad • R. Mendelsohn • C. R. Flach (✉)
Department of Chemistry, Rutgers University, 73 Warren Street
Newark, New Jersey 07102, USA
e-mail: flach@andromeda.rutgers.edu

G. Mao • R. M. Walters • M. C. Mack Correa
Johnson & Johnson Consumer Companies, Inc., 199 Grandview Rd.
Skillman, New Jersey 08558, USA

ABBREVIATIONS

C/C_o	Concentration/initial concentration
COM	Center of mass
D	Diffusion coefficient
DMSO-d	Dimethyl-d_6 sulfoxide
OA-d	Acyl chain perdeuterated oleic acid
SC	Stratum corneum
$v_{sym}CD_2$	Symmetric CD_2 stretching mode

INTRODUCTION

The majority of percutaneous penetration/permeation studies have focused on the ability of a substance to cross the stratum corneum (SC) barrier giving little consideration to competitive spreading and lateral diffusion that may take place simultaneously on the surface and within the SC, respectively. Along with these processes, the potential exists for the formation of a drug depot or reservoir in the SC which may have important consequences regarding dosing and controlled or timed-release (1,2). Lateral diffusion within the top layers of the SC and radial spreading mechanisms along surface furrows or glyphs are poorly defined although this information is of substantial pharmacological, toxicological, and cosmetic importance.

Diffusion in the SC is thought to take place *via* intercellular and/or transcellular routes, if permeant transport through skin appendages (hair follicles and glands) is ignored. Transport routes across and within the SC mostly depend on the size and lipophilicity of the exogenous agent (3). It is generally accepted that lipophilic compounds follow an intercellular route through the lipid matrix whereas hydrophilic compounds may diffuse through corneocytes and the lipid matrix, possibly including an aqueous pore pathway (1,4,5).

Fluorescence recovery after photobleaching (FRAP), employed for three decades to measure diffusion coefficients,

was used by Langer and co-workers (6) to measure the lateral diffusion of a series of nine fluorescence probes in extracted SC lipids. They derived diffusion coefficients ranging from 0.306×10^{-8} to 2.34×10^{-8} cm^2/s depending on probe molecular weight. More recently, fluorescence multiphoton tomography was employed in FRAP experiments performed on human SC *in vitro* (7). In another study, raster image correlation spectroscopy (RICS) based on multiphoton excitation fluorescence was used to evaluate local diffusion coefficients in excised human skin (8). Spatially resolved images of lateral diffusion coefficients were generated at different depths in the SC using amphiphilic and hydrophilic fluorescently labeled molecules. Diffusion in the SC was found to be very heterogeneous on a microscopic scale. Despite the substantial sensitivity of these techniques, there are some limitations for their usefulness in understanding lateral diffusion mechanisms in skin. First, the experiments require the presence of a fluorescent moiety which could have significant effects on molecular diffusion, especially in the heterogeneous environments of skin. Second, the use of fluorescence microscopy does not provide molecular structure information about the skin microenvironment, *e.g.*, fluorophore-induced structural changes in the molecular constituents of skin.

Tape stripping protocols with appropriate analytical methods have also been employed for monitoring lateral diffusion in SC. Early reports reveal differences in lateral diffusion *versus* depth of active agent penetration dependent on the delivery vehicle (9,10). More recently, Jacobi *et al.* (11) investigated the *in vivo* lateral spreading of UV filter substances and reported significant amounts in adjoining areas that result from spreading on the surface. Along similar lines, Schicksnus and Muller-Goymann (12) extracted concentric skin segments surrounding the site of application of ibuprofen to skin. Using HPLC detection, two phases of lateral diffusion were observed; accumulation in the central segment, followed by redistribution. Gee *et al.* (13) used a similar concentric tape stripping method to track both lateral spreading and SC penetration of caffeine, hydrocortisone and ibuprofen *in vivo*. They reported that lateral spreading behavior depends on the physicochemical properties of the applied drugs.

It is noted that the presence of furrows in the skin (glyphs) may invalidate the conclusions drawn from tape stripping experiments. Van der Molen *et al.* (14) reported the presence of non-stripped skin in the furrows after tape stripping 20 times. Indeed, glyphs have been shown to function as pathways for lateral spreading of topically applied substances (15,16) while their density and distribution vary with body site, age and environmental exposure (15,17,18). Hence, the influence of glyph distribution on lateral diffusion/spreading is not only an important experimental issue, but also has implications for pharmacology, toxicology, and cosmetics.

Vibrational spectroscopy-based methods (*i.e.* Fourier transform infrared (FT-IR) and Raman spectroscopies) offer some generic advantages compared to the fluorescence-based methods discussed above. As is well known, vibrational spectra provide molecular structure information from endogenous skin components in addition to the exogenous material whose diffusion is being monitored. Over the past 20 years, the development of both IR microspectroscopic imaging and confocal Raman microscopy have proven the feasibility of acquiring spatially resolved spectra from microtomed skin sections and intact skin (19–24). Although IR microscopic imaging has not been previously used to measure lateral diffusion kinetics in skin, studies demonstrating the feasibility of the experiment have indeed appeared. Gotter *et al.* (25) investigated the heterogeneous lateral distribution of the antipsoriasis drug dithranol in an artificial membrane. From our laboratories, Mao *et al.* (26) imaged the distribution of sodium dodecyl sulphate (SDS) across different skin regions. A useful advantage of IR imaging was realized from the fact that Beer's Law is obeyed in the IR, thereby permitting (in the example cited above) the determination of the SDS concentrations in the skin.

In the current study, we demonstrate the feasibility of mapping lateral spreading/diffusion in human SC with IR imaging. We image the spatial distribution and concentration of deuterated variants of the common permeation enhancers, oleic acid (OA) and dimethyl sulfoxide (DMSO). In addition to providing a temporal and spatial quantitative measure of OA concentration along networked furrows on the SC surface, images are generated for both permeants in relatively glyph-free regions. A range of diffusion coefficients for lateral transport based on Fick's second law are compared to the imaging data. Although the results do not directly distinguish between permeant spreading on the surface and that diffusing within the SC, the unique capabilities of IR spectroscopy permit us to detect perturbation to endogenous SC keratin structure for the DMSO experiments and changes in the OA spectra consistent with penetration.

MATERIALS AND METHODS

Materials

Trypsin (Type II-S from porcine pancreas), phosphate buffered saline, and perdeuterated oleic acid-d_{34} (OA-d), 98 atom % D were purchased from Sigma-Aldrich (St. Louis, MO). Dimethyl-d_6 sulfoxide (DMSO-d) was purchased from CDN Isotopes, Inc. (Quebec, Canada). Human abdominal skin (female donor, age 54) from a plastic surgery procedure (otherwise to be discarded), was obtained from dermatological offices following informed consent and approval of the institutional ethics committee. Samples were fast frozen with liquid nitrogen after removal of subcutaneous fat, cut into about 15×15 cm^2 pieces, and stored at −20°C for 6 months or less.

Methods

Isolation of SC. Skin samples of ~1×2 cm^2 surface area and thickness of ~2.5 mm were cut from a larger piece and defrosted on filter paper with the SC side up. The SC was cleaned with cotton swabs to remove surface fat, tape-stripped twice (Scotch Magic tape, 3 M) to remove most of the sebum, and then treated with 0.5% (w/v) trypsin buffer solution for 24 h at room temperature. The SC was isolated by peeling from the viable epidermis, rinsed with distilled water and then hair was removed. The SC was cut to the desired size, transferred onto a ZnSe IR window, and dried overnight under house vacuum.

IR Microscopic Imaging. IR images of skin were collected with a Perkin-Elmer Spotlight 300 system (PerkinElmer Life and Analytical Science, Inc., Waltham, MA) with an essentially linear array (16×1) of mercury-cadmium-telluride (MCT) detector elements. The system was purged with dry air (relative humidity ~12%) to minimize interference from water vapor rotation-vibration bands in the Amide I spectral region. The imaging protocol was to first acquire a control IR image of the SC prior to the application of either OA-d or DMSO-d. Most of the IR images were collected utilizing the transmission mode with a 25×25 μm^2 pixel size and 32 scans at a spectral resolution of 2 cm^{-1}. Occasionally an image was acquired using a 6.25×6.25 μm^2 pixel size (32 scans and spectral resolution of 8 cm^{-1}). Next, a finite application of 0.3 µL of OA-d or DMSO-d (the size of the drop was ~1.8–2.0 mm in diameter) was applied with the edge of the drop close to the imaging area used for the control image. The geometry of the set-up is shown in Fig. 1 where the visible micrograph of the SC appears yellow due to the ZnSe IR window. Finally, IR images were acquired as a function of time for 20–50 H after application. Each image required 1–2 H for acquisition and is labeled at the time image acquisition was complete. Experiments were repeated 3–4 times; typical data are presented. Image sizes were ~1,600× 800 μm^2, corresponding to 64 pixels in the x direction and 32 pixels in the y direction. Visible micrographs were obtained with the microscope integrated into the Spotlight 300 system.

Determination of IR Extinction Coefficients of OA-d and DMSO-d. OA-d was dissolved at known concentrations in methanol, octane and octanol. A fixed pathlength (15 µm) IR cell with CaF_2 windows was used to measure the absorbance of each standard. IR spectra were acquired with a Nicolet 6700 spectrometer (Thermo Electron Corporation, Madison, Wisconsin), 128 scans and using a spectral resolution of 2 cm^{-1}. A graph of the area of the symmetric CD_2 stretching ($v_{sym}CD_2$) band (obtained using ISys 3.1 software, Malvern Instruments, UK) as a function of molar concentration was plotted. Linear regression was used to find the best fit lines to the Beer's Law plots. The extinction coefficients (mol^{-1} dm^3 cm^{-1}) and correlation coefficients are as follows: methanol, 5653, 0.987; octane, 5222; 0.999 and octanol 6010, 0.996. The average of the three measured extinction coefficient values was used for quantitative analysis. When calculating OA-d concentration, we assume that the thickness (pathlength) of isolated human SC samples is 15 µm. A similar procedure was used to determine the extinction coefficient and concentration for DMSO-d based on the area of the asymmetric CD_3 stretching band. The extinction coefficients (mol^{-1} dm^3 cm^{-1}) and correlation coefficients are as follows: octanol, 201.8, 0.996 and propanol, 198.6, 0.999, respectively. The correlation coefficients demonstrate the high precision of using the symmetric CD_2 and asymmetric CD_3 stretching band areas to calculate OA-d and DMSO-d concentration in skin, respectively.

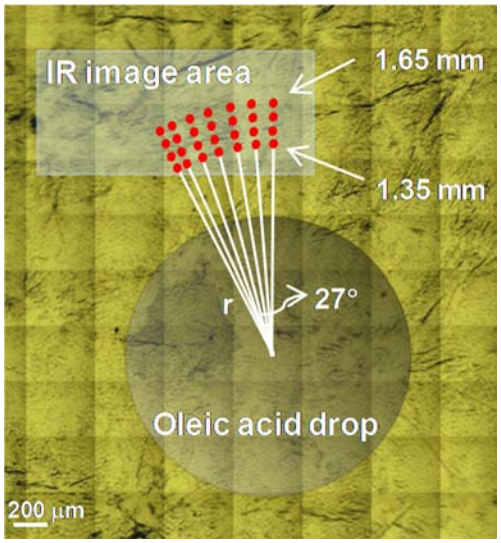

Fig. 1 Geometry of the experimental design and schematic of averaging the oleic acid-d concentration at various distances (1.35–1.65 mm) from the center of the source in a glyph-poor area. The schematic is shown on a visible image of isolated human SC on top of an IR ZnSe window.

IR Imaging Data Analysis. Vibrational microspectroscopic images were generated from IR spectral data using ISys 3.1 software (Malvern Instruments, UK). Image planes of spectral parameters (integrated peak areas, area ratios, and center of mass (COM) peak frequencies) were produced after linear baselines were applied in spectral regions of interest. Image planes of OA-d and DMSO-d concentrations were generated after applying the averaged extinction coefficient. Figures were generated with SigmaPlot 2000 (SPSS Inc., Chicago, IL).

Estimation of Diffusion Coefficients. The two dimensional diffusion equation is given as follows, assuming the diffusion coefficient, D, is constant and [C] is the concentration of the diffusing molecule:

$$\frac{\partial^2[C]}{\partial x^2}+\frac{\partial^2[C]}{\partial y^2}=\frac{1}{D}\frac{\partial[C]}{\partial t}$$

The concentration at a distance "r" where $r = (x^2 + y^2)^{1/2}$ from a point source on an infinite plane is given by:

$$[C]=\frac{M}{4\pi Dt}e^{(-r^2/(4Dt))}$$

where M is the total amount of the diffusing substance and t is time. When an instantaneous cylindrical source with a radius (r) of 1,000 μm (as observed in our experiments) is left to diffuse throughout an infinite plane surface, Crank (27) has shown the corresponding result to be:

$$\frac{C}{C_o}=\frac{1}{2Dt}e^{(-r^2/(4Dt))}\int_0^{1000}\left\{e^{(-w^2/(4Dt))}I_o(rw/2Dt)\right\}wdw$$

where I_o is the modified Bessel function of the first kind of order zero, with an argument of (rw/(2Dt)) and C_o is the initial concentration. The equation was evaluated with Mathcad 2001 (PTC, Needham, MA).

Determination of Initial Concentration. A solution of molar ratio of 1:19 deuterated oleic acid:protonated oleic acid was prepared to measure initial OA-d concentration. 0.3 μL of the solution was placed on a piece of isolated SC and a visible image of the drop was taken using the Spotlight instrument. Infrared spectra (point mode, aperture size: 100 μm^2) were acquired at a series of points inside the OA drop. The integrated area of the $\nu_{sym}CD_2$ band was calculated at each point and then averaged (A). The radius of the OA drop was measured from the visible image. Assuming the drop is a perfect cylinder, the height of the cylinder which is the pathlength (l), can be calculated based on the volume and area. According to Beer's law, the initial concentration was calculated from: $C_o = (A/(E_x l))F$, where E_x is the molar extinction coefficient and F is an adjustment factor based on the molar ratio (total moles/OA-d moles) of 20. This molar ratio was chosen to keep the $\nu_{sym}CD_2$ band on scale based on the IR imaging detector sensitivity. A similar procedure was used to determine the initial concentration of DMSO-d.

RESULTS

A schematic depiction of the IR imaging lateral diffusion experiment, overlaid on a visible micrograph of the SC, is shown in Fig. 1. The typical area over which IR spectra are acquired is ~0.5×1.0 mm. OA-d was applied as a 0.3 μL drop (pure liquid). Usually, the front edge of the source drop is ~300 μm away from the area of the rectangular IR image plane; however occasionally the source drop area overlapped this image plane. As is evident in the figure, separate regions of the SC appear to be nearly furrow-free or contain several networked furrows. Data are presented herein from both regions, although we cannot rule out that smaller, non-visible glyphs may be present in the glyph-poor areas. Representative radial distances from the center of the source over which diffusion coefficients in a glyph-poor area were evaluated are marked in the figure.

OA-d Diffusion Experiments. IR and visible images were collected from the same area as a function of time following application of the OA-d drop to the SC surface. Representative spectra depicting the appearance of OA-d at a particular site at a few time points following application to the surface are shown in Fig. 2a. Important spectral features are labeled in the Figure. The spectra are of high quality depicting a S/N ratio of ~200 for the Amide II vibration near 1,550 cm^{-1}. Of particular interest in the evaluation of the diffusion process is the time evolution of the spectral intensity in the CD_2/CD_3 stretching region (2,000–2,300 cm^{-1}). This spectral region is shown enlarged in Fig. 2b for spectra acquired at 0, 4.5, 24.5, and 50.5 H (top to bottom) following application. The integrated band intensity of $\nu_{sym}CD_2$ (~2,100 cm^{-1}) was used to determine the concentration of OA-d (as described in the Experimental section).

Several IR images displaying the spatial distribution of the OA-d concentration on and/or within the isolated SC as a function of time after application are shown in Fig. 3. A visible image of this glyph-rich region of the SC acquired before the OA-d was applied is included in the figure. The source droplet was applied with its edge ~0.2 mm from the bottom left-side of the image area as depicted in Fig. 3. It appears, from the very high OA-d concentrations in the lower portion of the images, that the droplet of OA-d has spread into the imaged area (most likely between 5 and 11 H) during IR data acquisition. Since spectra were collected in the transmission mode, the peak intensities obey Beer's law. Color codings are converted to oleic acid concentrations as depicted on the scale bar in the figure. The scale bar upper range has been manually set to highlight concentration variations in the IR images that track the glyphs shown in the visible micrographs. An overlay of the visible image in the top row (transparent) with a concentration image taken at 55 H is displayed in the bottom row (right) with the intent of emphasizing the manner in which the concentration profile follows the glyph network in the SC. The time evolution of the concentration images suggests that the OA-d is wicking or spreading predominantly within the grooved glyphs of the SC. At early times (<8 H), OA-d is first observed to spread into the vertical furrow in the bottom left-

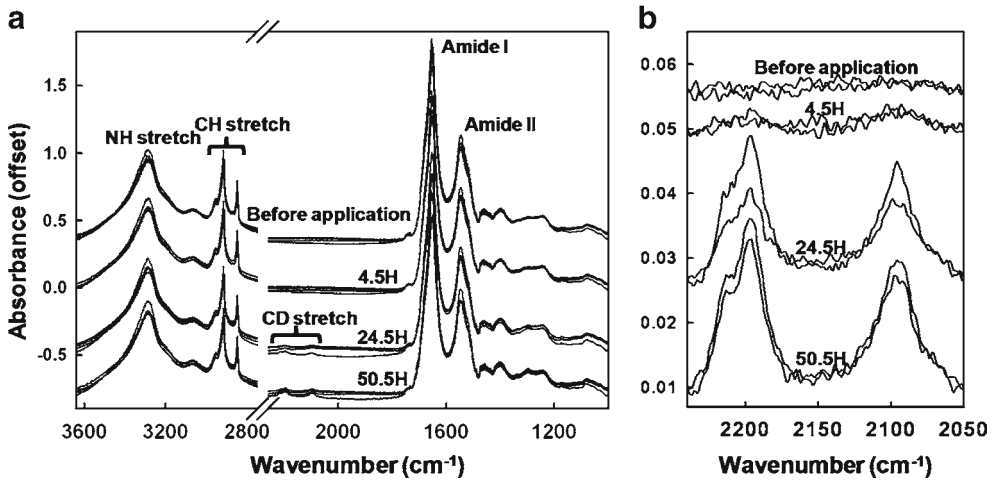

Fig. 2 Overlaid, unprocessed, single pixel (25 μm^2) IR spectra of OA-d treated SC at 1.35 mm from the center of the source in a glyph-poor area. (**a**) representative spectra offset at 0, 4.5, 24.5 and 50.5 H following OA-d application. Spectral features of interest are labeled. (**b**) Similar spectra as shown in (**a**) highlighting the CD_2 stretching region (2,050–2,240 cm^{-1}). The spectra are baseline corrected at 2,250 and 2,059 cm^{-1}.

hand side of the visible image. At times ≥8.5 H, the presence of OA-d becomes apparent in a second glyph on the bottom right. As the concentration of OA-d increases to ≥0.4 M in the lower portion of the image (≥8.5 H), the glyph network in the top portion begins to fill with OA-d, reaching concentrations of ~0.15 M at ≥27.5 H. Concentration profiles in glyph-rich areas were explored further.

OA-d concentration along a nearly continuous set of furrows, as shown in the visible image in Fig. 4a (visible image from Fig. 3 is cropped and rotated with source droplet located

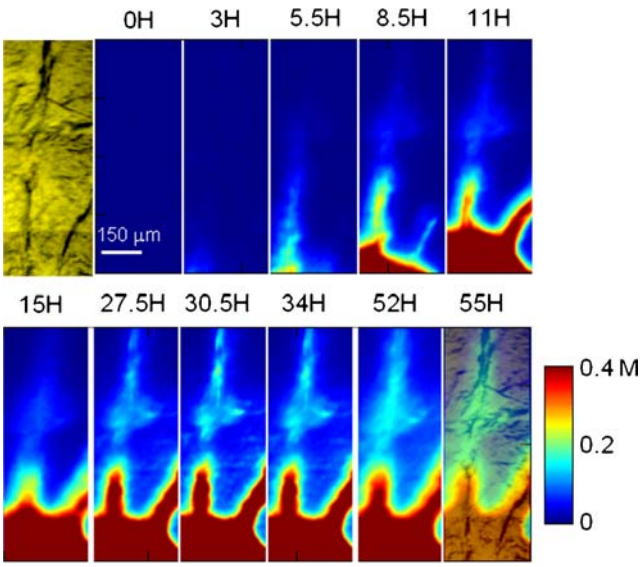

Fig. 3 IR images of OA-d concentration as function of time in a glyph-rich area (6.25 μm^2 pixel size). The smaller pixel size is used to better visualize the transport within the glyphs. The source droplet was applied with its edge ~0.2 mm from the bottom left-side of the image area. The concentration range of 0–0.4 M is shown for better viewing of OA-d diffusion within the glyphs. The concentration of OA-d is calculated based on the symmetric CD_2 stretching band area according to Beer's Law. The 2,059–2,132 cm^{-1} region is baseline corrected and integrated. The image size is 0.30 × 0.80 mm^2. The visible image of the SC (*top left*) is taken before OA-d application. An overlay of the visible image (transparent) with a concentration image taken at 55 H is displayed in the bottom row (*right*).

at left side), is displayed in Fig. 4b as a function of distance from the source and time after application. There are a few regions within the glyphs at specific distances from the source center (black arrows at ~1.45, 1.85, and 1.95 mm) that appear to go through a concentration maximum with time, at 30.5 H. The visible image is the darkest at these locations which may reflect a maximum depth in the glyphs at these particular points. An additional upsurge in concentration is evident at earlier time points for the 1.45 mm distance at 8.5–11 H. The stabilizing of OA-d concentration to ~0.15 M (as noted above) is evident for the two longest time points over a range of distance from the source (1.55–1.95 mm).

Concentration profiles are plotted across a glyph at the same distance from the source center (~1.4 mm) in an attempt to evaluate whether transport along a glyph can be discerned from diffusion within the SC lipid layers. The red line in the visible image (Fig. 4a) marks the approximate location of those spectral pixels chosen for the concentration profiles shown in Fig. 4c. At this location, the approximate width of the furrow appears to be ~20 µm in the visible image. As observed in Fig. 4c, OA-d concentrations are strongly influenced by the presence of the glyph within 20 µm of its center, reaching a maximum at 30.5 H, as mentioned above for concentration within the glyph area. The influence is not as strong at 31.3 µm away from the center and at greater distances the temporal concentration behavior appears to have two phases. There is a relatively rapid initial increase in concentration from 0 to 15 H, followed by a slower rate of increase for the remainder of the experiment. It is tempting to speculate that at distances greater than ~30 µm from the glyph center, the OA-d has penetrated into the SC to the point that the temporal concentration profiles are governed by its lateral diffusion within the SC lipid layers. This point will be expanded upon in the Discussion.

IR images presented in Fig. 5a display the time evolution of OA-d concentration for a lateral diffusion experiment in a SC region that is relatively glyph-free. The edge of the source

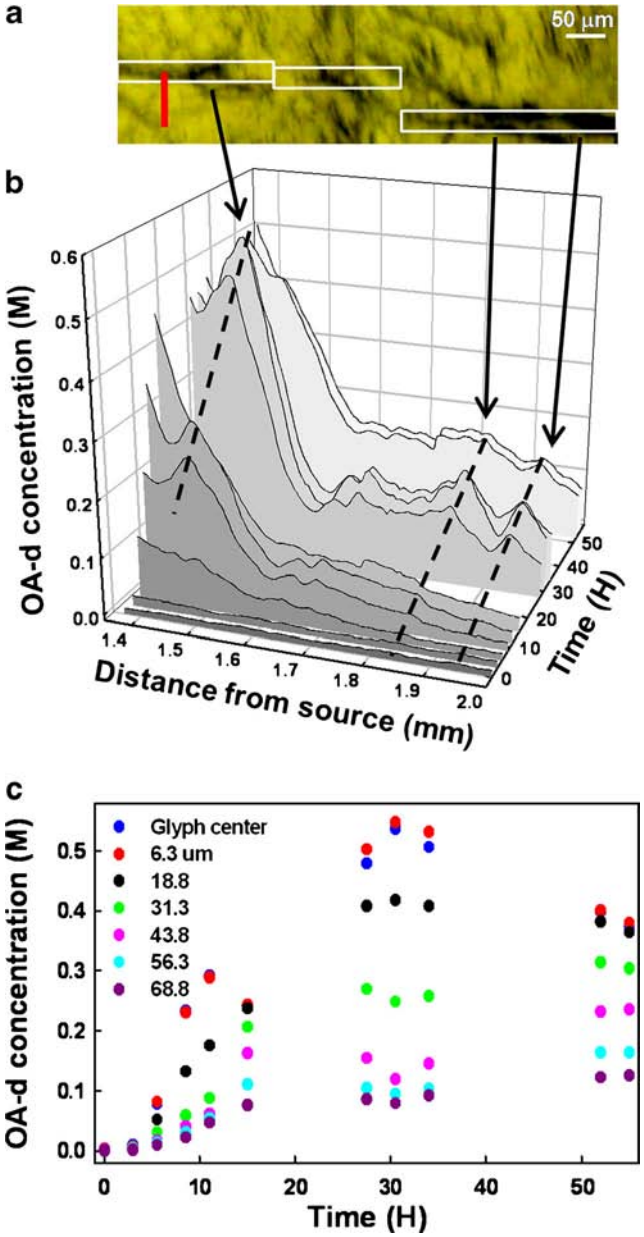

Fig. 4 OA-d concentration as function of time and distance from the source in glyph-rich regions. (**a**) The visible image of the SC from Fig. 3 has been cropped and rotated to facilitate comparison of glyph locations with the concentration plot shown in (**b**). The center of the OA-d droplet was located at ~1.37 mm from the left-hand edge of the cropped image. (**b**) Three dimensional plot of OA-d concentration as function of time and distance from the source center along glyphs. The plotted concentrations are averaged across three pixels (shown within the *white rectangles* in (**a**)). The *arrows and dashed lines* are shown to guide the eye (see text). (**c**) OA-d concentration as function of time at several distances from glyph center (position shown as *red line* in (**a**)), all ~1.4 mm from the source center.

droplet in this experiment is located ~200 µm below the right hand side of the IR image area as shown in Fig. 1 and its shape does not appear to change over the time period of the experiment. OA-d can be observed diffusing into the lower right hand portion of the IR image within the first 2 H after application (Fig. 5a). As the spatial distribution of OA-d concentration increases with time, a finger-like feature of relatively high OA-d concentration is initially observed at ~22 H (white arrow), spatially aligned with a small glyph in the lower right hand corner of the visible image (not shown). The projection remains as a distinct area of higher concentration until the concentration in the surrounding area increases (at times ≥47 H) to approximately the same level (≥0.05 M). Fig. 5b displays averaged OA-d concentration as a function of time for particular distances from the source as delineated in Fig. 1. Each concentration value is averaged from ~30 spectra for each time period. It is likely that the "error" bars (standard deviation) predominantly reflect concentration differences due to the native heterogeneity of the SC. In addition, it is readily apparent that the OA-d concentrations in the glyph-poor areas are at least an order of magnitude less than those in the glyph-rich areas for comparable distances from the source (compare to Fig. 4b).

IR images of OA-d concentration in glyph-poor areas were analyzed further and compared to results from Crank's solution of lateral diffusion in two dimensions (27) to obtain a range of diffusion coefficients which best describe the experimental data. The outcome is plotted in Fig. 5c as radius *vs.* time. The OA-d detection limit of 5 mM based on the $\nu_{sym}CD_2$ band was used to obtain the radii values shown in the graph. The experimental results are essentially bracketed by the calculated values shown in the figure. The diffusion coefficients that seem to track the experimental data appear to decrease with time; ranging from $\sim 1\times10^{-8}$ cm^2/s for shorter times to $\sim 3\times10^{-9}$ cm^2/s for longer times.

The use of perdeuterated OA permits the detection of permeant-induced changes in endogenous SC lipid acyl chain conformation *via* frequency shifts in the methylene stretching bands. In a similar manner, frequency shifts in the CD_2 stretching bands can indicate interaction between the disordered OA-d chains and the highly ordered lipids of the SC. Overall, the lower the frequency, the greater the acyl chain conformational order. No sign of alteration to endogenous structure was detected in the OA-d treated SC samples; however, measurable changes in the $\nu_{sym}CD_2$ suggest that at least a portion of the OA-d has penetrated into the SC. Since the transmission mode is utilized to acquire the IR images, the resultant spectra are a weighted average of OA-d residing on the surface and that which has penetrated into the SC. As shown by the overlaid spectra in Fig. 6, the $\nu_{sym}CD_2$ for OA-d decreases by ~1.5 cm^{-1} comparing the frequencies immediately after a drop was placed on the SC surface and in octanol solutions (~2098.6 and 2099.0 cm^{-1}, respectively) with frequencies measured in glyph-poor regions of the SC at various time points after application (2097.4 and 2097.5 cm^{-1} after 4.5 and 29 H, respectively). Similar changes are observed for the $\nu_{asym}CD_2$ (not shown). A 1.5 cm^{-1} shift covers approximately a quarter of the wavenumber range available for this vibrational mode and indicates that a moderate

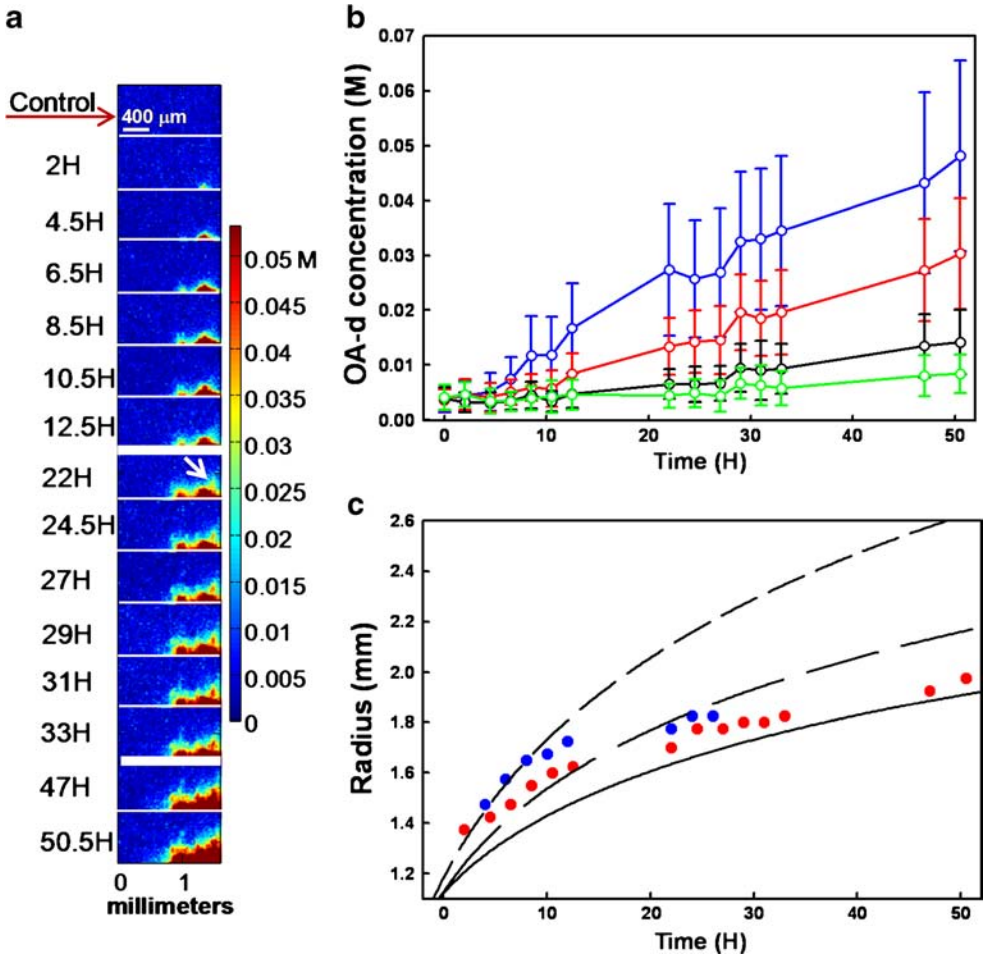

Fig. 5 OA-d concentration as function of time in a relatively glyph-free area. (**a**) IR images (25 μm^2 pixel size, 1.60 × 0.80 mm^2 image size) displaying the time evolution of OA-d concentration. The edge of the source droplet is ~0.2 mm below the bottom right-hand side of the image. The *white arrow* in the image at 22 H marks a finger-like feature possibly due to a small glyph. (**b**) Averaged OA-d concentration (± standard deviation) as function of time at particular distances from the source center. Each concentration is the average of ~30 pixels as depicted in Fig. 1 for each distance from the source center (in mm): *blue*: 1.35; *red*: 1.45; *black*: 1.55; *green*: 1.65. (**c**) The expanding radius of oleic acid due to diffusion as a function of time for duplicate experiments (*red and blue filled circles*) compared to a range of diffusion coefficients obtained from Crank's solution of Fick's second law for lateral diffusion in two dimensions (see Methods section for details). The radii values are obtained based on OA-d detection limit of 5 mM. Diffusion coefficients are as follow: *solid line*, 0.3e–8 cm^2/s; *long dashed line*, 0.5e–8 cm^2/s; *short dashed line*, 1.0e–8 cm^2/s.

degree of acyl chain conformational ordering has taken place as the OA-d likely interacts with the more highly ordered SC lipids. In earlier reports from our laboratory, both the ν_{asym} and $\nu_{sym}CD_2$ have been used as indicators of acyl chain perdeuterated permeant penetration and interaction with SC lipids (26,28).

DMSO-d Diffusion Experiments. In contrast to the OA-d experiments discussed above, IR imaging experiments of DMSO-d lateral diffusion in the SC directly detected structural perturbation to endogenous SC protein. Figure 7 displays overlaid IR spectra from imaging experiments at various time points after the application of DMSO-d to SC. In addition to bands specific to DMSO-d (Fig. 7a), *i.e.*, CD_3 stretch (2,050–2,250 cm^{-1}) and S=O stretch (1,000–1,100 cm^{-1}), the presence of a shoulder (~1,626 cm^{-1}) on the low frequency side of the Amide I band was observed (Fig. 7b), indicating a fair degree of DMSO-induced keratin denaturation. In the IR spectra of the SC, keratin is the major contributor to absorbance in the Amide I region with minor contributions arising from small amounts of various SC proteins and the ceramide Amide group. The overall symmetric shape of the Amide I band and frequency position (~1,650 cm^{-1}) before DMSO-d application are indicative of keratin's helical structure. However, after DMSO-d is applied, the increase in intensity at ~1,626 cm^{-1} denotes the formation of β-sheet structure. Similar DMSO-induced helix to sheet transitions have been previously observed by IR in human SC and isolated human corneocytes (29,30) and the detection of keratin denaturation herein provides proof that DMSO has penetrated into the corneocytes within the SC. The apparent splitting at the Amide I peak maximum, evident in Fig. 7b, is caused by

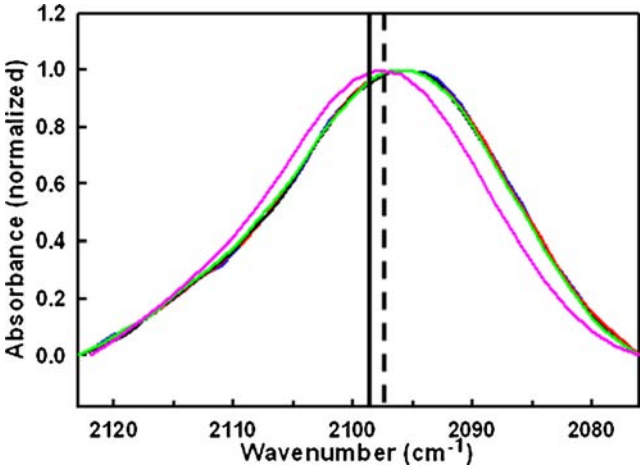

Fig. 6 Overlaid spectra of the symmetric CD_2 stretching band at particular time points after OA-d application (1.35 mm away from the source center) compared to that of the OA-d droplet on the SC obtained within 5–10 min after application (*pink*). Time after application (in H): *blue*, 4.5; *red*, 12.5; *black*, 29.0; *green*, 50.5. The spectral region is baseline corrected at 2,123–2,076 cm^{-1} and normalized to highlight the frequency shift. The *vertical solid line* is the COM frequency for the droplet (2098.6 cm^{-1}); whereas the *dashed line* is the averaged COM frequency for the four different time points (2097.5 cm^{-1}).

saturation of the MCT IR detector due to the thickness of the SC (~15 μm).

IR images of the time evolution of DMSO-d lateral diffusion in a glyph-poor SC region (see visible image in Fig. 8a) are displayed in Fig. 8b where DMSO-d concentration is observed to go through a maximum 3.0–6.0 H after application. In addition, the source droplet of DMSO-d vanishes from the visible images within the first 2 h after application. The circular region of high DMSO-d concentration (deep red) evident in the center of the lower half of the images taken at ≥7.5 H is suggested to arise from a hair follicle. Images depicting the relative amount of keratin denaturation are displayed in Fig. 8c. A time delay between the maximum DMSO-d concentration in a particular spatial region and keratin denaturation is evident when the images are compared and is shown more clearly in Fig. 9a. In this figure, the time evolution of DMSO concentration (C/C_o) is plotted along with the relative amount of β-sheet at a position 1.35 mm away from the center of the source. Each data point shown is measured from the average of 14 spectra. A delay time of 3–4.5 H is observed between increasing DMSO-d concentrations and observable β-sheet formation. Under the current experimental conditions, keratin denaturation does not appear to be reversible with time as DMSO-d concentration decreases. This observation will be explored in future experiments as keratin denaturation was shown to be largely reversible after corneocyte exposure to high relative humidity (30). Thus, the observed structural perturbation to keratin in the SC is consistent with a transcellular penetration route for DMSO which includes a pathway through both the lipid matrix and corneocytes.

A comparison between experimental and calculated DMSO-d concentrations as a function of time at a position 1.35 mm away from the source is shown in Fig. 9b along with comparable OA-d concentrations for the glyph-poor experiment. The calculated curves for a wide range of diffusion coefficients (5×10^{-10} to 2×10^{-7}) are shown. There is a marked difference between the experimental results for the two permeants. Although the magnitudes of the calculated C/C_o values for the larger diffusion coefficients ($\geq5\times10^{-8}$) at early times (<10 H) are greater than that of the experimental values, the behavior of the calculated curves with a maximum C/C_o (peak flux) at relatively early times are similar to the DMSO-d experimental results.

DISCUSSION

Early studies of model lipid and human red blood cell membranes report that the rate of lateral diffusion is more rapid

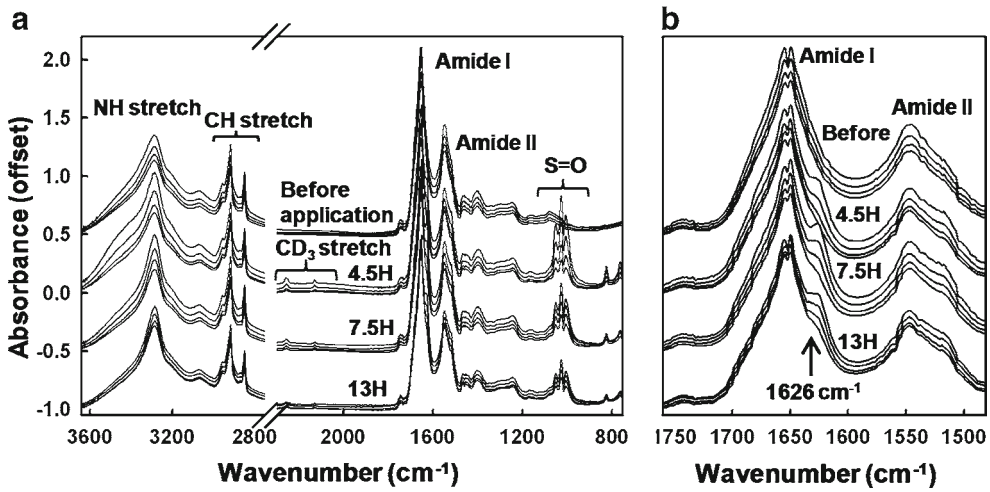

Fig. 7 IR spectra of DMSO-d at ~1.0 mm from the center of the source. (**a**) Offset representative spectra at 0, 4.5, 7.5 and 13 H following DMSO-d application. Bands of interest are labeled. (**b**) Enlarged Amide I/II region (baseline corrected at 1,450–1,750 cm^{-1}) highlighting the evolution of a shoulder at ~1,626 cm^{-1} indicative of keratin denaturation (see text for details) after DMSO-d exposure.

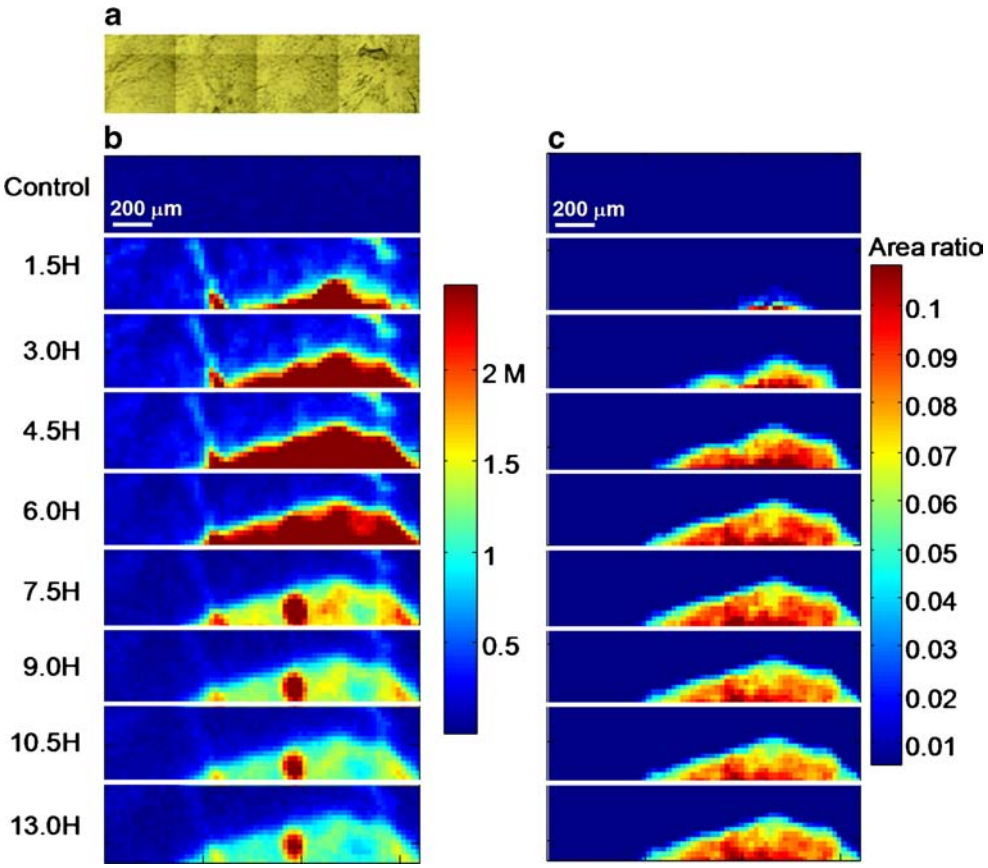

Fig. 8 IR images of DMSO-d diffusion in a relatively glyph-poor SC region as function of time. (**a**) Visible image of the SC in the IR imaging area (25 μm^2 pixel size, 1.60×0.40 mm^2 image size). The source droplet was deposited at the lower right side and its edge impinged within the image area by ~50 mm with an initial radius of 0.9 mm. (**b**) IR images of DMSO-d concentration before and after application as function of time. The concentration range of 0–2.47 M is shown for better viewing of DMSO-d diffusion. DMSO-d concentration is calculated based on the asymmetric CD_3 band area (baseline corrected over 2,281–2,232 cm^{-1}) according to Beer's Law. (**c**) IR images of the relative amount of keratin denaturation measured by the integrated area ratio of the β-sheet shoulder (1,644–1,590 cm^{-1}) to the CH stretching region.

than transbilayer transport (31,32). In skin, relatively few studies have attempted to track both the penetration and lateral diffusion of drugs. Most of those studies employ tape stripping protocols that have the potential to provide information regarding both penetration and lateral diffusion of exogenous agents albeit, confined to the SC region of skin (see Introduction). One very recent *in vitro* study (2), included the tape stripped SC layers, deeper skin layers and lateral skin parts. In general, although the analytical techniques utilized in these studies provide precise quantitative measures of permeant concentrations, information regarding possible perturbation to endogenous SC structure is lacking. Endogenous molecular structure information is also lacking in fluorescence-based diffusion measurements.

The IR imaging method we demonstrate here for tracking lateral diffusion of exogenous materials in the SC offers some advantages. One major advantage of IR spectroscopy is that there is no need to attach a chromophore to the exogenous agent under study. Additionally, IR spectra provide molecular structure information from endogenous skin components and the exogenous material whose diffusion is being monitored. In the current study, we take advantage of deuterated analogues to isolate the C-D stretching modes of the molecule of interest. This also frees up the C-H stretching region of skin lipids yielding information regarding permeation mechanisms. Depending on the IR spectrum of the exogenous agent, other spectral regions may also remain free from spectral overlap, as demonstrated herein by the DMSO-induced endogenous keratin denaturation detected in the Amide I region. Finally, when IR imaging is conducted in the transmission mode and the sample has a uniform thickness, Beer's Law provides quantitative concentration values for the exogenous agent.

The concentration profiles depicted in a glyph-rich region in Fig. 3 clearly reveal that the predominant contribution to OA-d lateral spreading arises from these structures. The role of glyphs as pathways for lateral diffusion on the skin surface has been previously reported (15,16) although we believe the IR images shown here (Fig. 3) are the first to report the spatial distribution of the concentration of exogenously applied material. Lateral transport along the glyphs not only competes with penetration but also provides a reservoir of exogenous material in regions removed from the site of application. Thus as glyph density is known to be dependent on body site, skin exposure, and aging (15,17,18), the consequences of these observations should be of significant interest for those involved with transdermal and cutaneous drug delivery, toxicology, and personal care or cosmetic applications. The phenomenon of glyph storage may partially account for age-related chronic skin dryness as glyph structures become less dense with age,

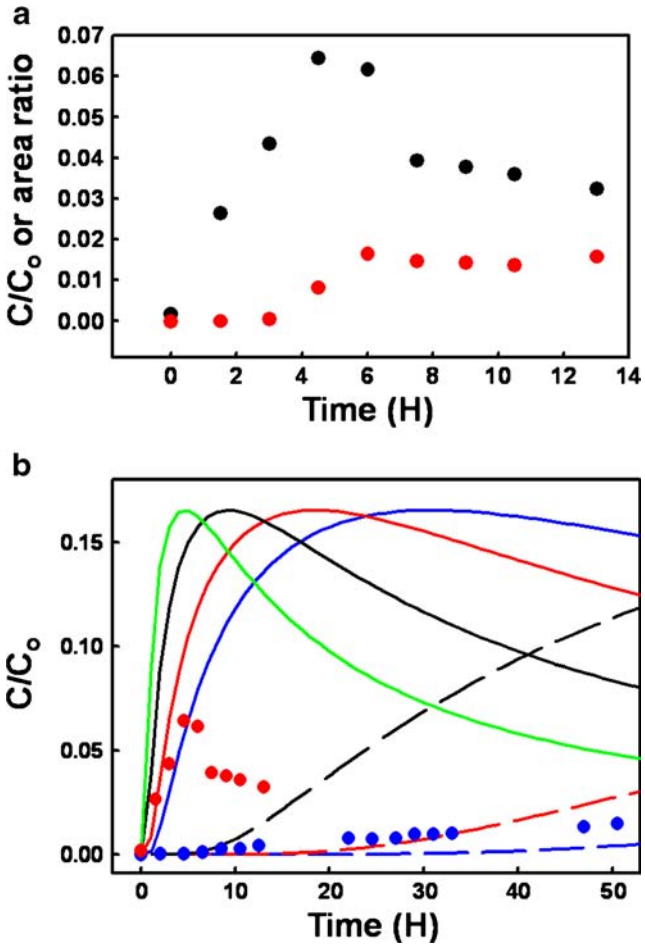

Fig. 9 (**a**) Overlay of DMSO-d concentration as C/C_o where C_o is the initial DMSO-d concentration and a relative measure of keratin denaturation (as described for Fig. 8c) as a function of time at a position 1.35 mm away from the source center highlighting the time-delay of protein denaturation. Each data point shown is the average of 14 spectra (*black*: DMSO-d C/C_o; *red*: keratin denaturation). (**b**) Comparison between experimental (DMSO-d, *red* and OA-d, *blue symbols*; both relatively glyph-poor regions) and calculated concentrations (C/C_o) as a function of time at 1.35 mm away from the source center. Calculated concentrations are obtained from Crank's equation (see text for details). Diffusion coefficients for the simulated plots are as follows: *solid lines* (source radii: 0.9 mm): *blue*: 0.3e–7 cm^2/s; *red*: 0.5e-7; *black*: 1.0e-7; *green*: 2.0e-7; *dashed lines* (source radii: 1 mm): *blue*: 0.5e–9 cm^2/s; *red*: 1.0e-9; *Black*: 3.0e-9

thereby reducing the reservoir in skin for topically applied hydration products.

Attempts were made to fit the glyph-rich OA-d experimental data with empirical engineering models for the kinetics of liquid spreading in V-shaped grooves (33), however, these models are based on complete wetting which does not apply to the current OA-d experiment. In addition, we have observed that absorption into the SC occurs while the OA-d spreads along the glyphs, a complication not accounted for in the engineering models cited above. Based on these two differences between models and experiment, it seems reasonable that the models consistently predicted much larger radii of spreading compared to our experimental data (results not shown). OA-d penetration in glyph-rich regions can be monitored in a manner similar to the glyph-poor OA-d experiments discussed above (Fig. 6). The frequencies of $v_{sym}CD_2$ suggest that a fair portion of the OA-d in the vicinity of the glyphs has penetrated into the SC.

Alterations to endogenous SC lipid chain conformational order determined from shifts in CH_2 stretching frequencies were not detected in the OA-d treated SC samples. This is consistent with a recent publication from our laboratories (34) where IR imaging was employed to monitor OA-d penetration. In that study which used microtomed sections, OA-d was shown to permeate to the dermal/epidermal junction with no significant differences observed in endogenous SC lipid ordering. Seemingly in contrast, endogenous chain disordering was detected in *in vivo* attenuated total reflectance (ATR) IR measurements of OA-d penetration in human skin (35) (34). However ATR-IR only probes the outer few microns of the SC and when this measurement was combined with tape stripping, the perturbation to endogenous lipid structure was indistinguishable from an untreated skin region after a few tape strips. In the current experiment, the absence of a frequency shift is likely due to the use of the transmission mode for IR spectral acquisition which produces spectra that reflect the average of the endogenous acyl chain conformation over the entire SC thickness. We also cannot rule out that a portion of the OA-d may be penetrating through slightly less ordered endogenous SC lipid regions, *i.e.* the grain borders described by Forslind (36) or through an altogether different route, eg., aqueous pores, although it is likely that these pathways would not produce the observed CD_2 frequency shifts.

In glyph-poor regions of the SC where we assume the OA-d has mostly penetrated, its distribution is reasonably well approximated by Crank's solution (27) of Fick's Second Law. A range of diffusion coefficients ($0.3–1\times10^{-8}$ cm^2/s) bracket the experimental data. Although this range for D is quite similar to that previously reported for the lateral diffusion of a series of fluorescent probes in extracted SC lipids ($0.3–2\times10^{-8}$ cm^2/s (6)) and for the average D of hydrophilic and amphiphilic fluorescent probes in human SC ($0.3–0.8\times10^{-8}$ cm^2/s (8)), we may be underestimating the diffusion coefficient due to penetration or diffusion in the Z-dimension given that the isolated SC is ~15 microns thick. In addition, as noted above, the range of diffusion coefficients that bracket the experimental data (see Fig. 5) appears to decrease with time. More rapid lateral diffusion at earlier time points may also be due to some initial wicking or spreading of OA-d across the SC surface prior to penetration into the SC. Other discrepancies may arise when utilizing Crank's model because the SC's native heterogeneity is not consistent with the model's assumption of isotropic media. In addition, the source is not a perfect cylinder; however it is the closest geometric form for which we have found a closed solution for the diffusion equation.

Estimation of lateral diffusion coefficients for DMSO-d in the SC *via* the current IR imaging experiment is hampered by the relatively quick diffusion of this well known permeation enhancer compared to the timescale of our measurement. The data presented in Fig. 9 appear to indicate that D values in the 10^{-7} cm^2/s range may be appropriate. The design of future imaging experiments is being modified to sample smaller areas of the SC on a faster timescale, along with the possible addition of confocal Raman microscopy measurements to probe "z" direction diffusion. The difference in the magnitude of calculated C/C_o (for D in the 10^{-7} cm^2/s range) compared to the experimental data is thought to be due to permeation of DMSO-d throughout the SC thickness as mentioned above. Extending confocal Raman microscopy measurements to intact, full thickness skin biopsies would also offer a more physiologically relevant experiment.

One result of the DMSO-d experiments provides a clear demonstration of the major advantage of utilizing vibrational spectroscopic imaging for diffusion studies in skin. The ability to detect changes in the structure of endogenous SC components suggests the pathway/mechanism of the diffusing substance as is evident in Fig. 7. Alterations to keratin's secondary structure in response to DMSO-d diffusion are strongly indicated by the low frequency shoulder that arises on the Amide I band (Fig. 7b) revealing an intercellular diffusion pathway.

In summary, the inherent complexities of the SC constrain the ability to model the system accurately. However the approach demonstrated here offers the potential to identify permeant-induced perturbations to specific endogenous SC species thereby providing useful and otherwise unavailable information for elucidating transport mechanisms.

CONCLUSION

Utilizing IR imaging to track the spatial and temporal distribution of exogenous agents in isolated human stratum corneum provides insight into competitive lateral diffusion processes. Transport along networked furrows is shown to be the dominant mode of lateral diffusion for the lipophilic permeation enhancer oleic acid. As such, the glyphs provide a reservoir of exogenous material for penetration and further lateral diffusion. The acquisition of a complete IR spectrum at each sampling point provides unique molecular level information with respect to changes in the structure of endogenous SC constituents and exogenous agents as they interact with the SC. Thus, the observation of DMSO-induced keratin denaturation facilitates the elucidation of a transcellular pathway for this permeation enhancer. Finally, since the IR imaging experiments are conducted in the transmission mode, the application of Beer's law provides quantification of exogenous agent concentrations. This, in turn, facilitates the inherently difficult estimation of diffusion coefficients.

ACKNOWLEDGMENTS AND DISCLOSURES

This work was generously supported by Johnson & Johnson Consumer Companies, Inc.

REFERENCES

1. Jepps OG, Dancik Y, Anissimov YG, Roberts MS. Modeling the human skin barrier - towards a better understanding of dermal absorption. Adv Drug Deliv Rev. 2013;65(2):152–68.
2. Selzer D, Hahn T, Naegel A, Heisig M, Kostka KH, Lehr CM, *et al.* Finite dose skin mass balance including the lateral part: comparison between experiment, pharmacokinetic modeling and diffusion models. J Control Release. 2013;165(2):119–28.
3. Potts RO, Guy RH. Predicting skin permeability. Pharm Res. 1992;9(5):663–9.
4. Johnson ME, Blankschtein D, Langer R. Evaluation of solute permeation through the stratum corneum: lateral bilayer diffusion as the primary transport mechanism. J Pharm Sci. 1997;86(10):1162–72.
5. Menon GK, Elias PM. Morphologic basis for a pore-pathway in mammalian stratum corneum. Skin Pharmacol. 1997;10(5–6):235–46.
6. Johnson ME, Berk DA, Blankschtein D, Golan DE, Jain RK, Langer RS. Lateral diffusion of small compounds in human stratum corneum and model lipid bilayer systems. Biophys J. 1996;71(5):2656–68.
7. Anissimov YG, Zhao X, Roberts MS, Zvyagin AV. Fluorescence recovery after photo-bleaching as a method to determine local diffusion coefficient in the stratum corneum. Int J Pharm. 2012;435(1):93–7.
8. Brewer J, Bloksgaard M, Kubiak J, Sorensen JA, Bagatolli LA. Spatially resolved two-color diffusion measurements in human skin applied to transdermal liposome penetration. J Investig Dermatol. 2013;133(5):1260–8.
9. Ashworth J, Watson WS, Finlay AY. The lateral spread of clobetasol 17-propionate in the stratum corneum in vivo. Br J Dermatol. 1988;119(3):351–8.
10. Chambin-Remoussenard O, Treffel P, Bechtel Y, Agache P. Surface recovery and stripping methods to quantify percutaneneous absorption of caffeine in humans. J Pharm Sci. 1993;82(11):1099–101.
11. Jacobi U, Weigmann H-J, Baumann M, Reiche A-I, Sterry W. Lateral spreading of topically applied UV filter substances investigated by tape stripping. Skin Pharmacol Physiol. 2004;17(1):17–22.
12. Schicksnus G, Muller-Goymann CC. Lateral diffusion of ibuprofen in human skin during permeation studies. Skin Pharmacol Physiol. 2004;17(2):84–90.
13. Gee CM, Nicolazzo JA, Watkinson AC, Finnin BC. Assessment of the lateral diffusion and penetration of topically applied drugs in humans using a novel concentric tape stripping design. Pharm Res. 2012;29(8):2035–46.
14. van der Molen RG, Spies F, van't Noordende JM, Boelsma E, Mommaas AM, Koerten HK. Tape stripping of human stratum corneum yields cell layers that originate from various depths because of furrows in the skin. Arch Dermatol Res. 1997;289(9):514–8.
15. Jacobi U, Schanzer S, Weigmann H-J, Patzelt A, Vergou T, Sterry W, *et al.* Pathways of lateral spreading. Skin Pharmacol Physiol. 2011;24(5):231–7.
16. Dussaud AD, Adler PM, Lips A. Liquid transport in the networked microchannels of the skin surface. Langmuir. 2003;19(18):7341–5.
17. Jacobi U, Chen M, Frankowski G, Sinkgraven R, Hund M, Rzany B, *et al.* In vivo determination of skin surface topography using an optical 3D device. Skin Res Technol. 2004;10(4):207–14.

18. Lavker RM, Kwong F, Kligman AM. Changes in skin surface patterns with age. J Gerontol. 1980;35(3):348–54.
19. Zhang G, Moore DJ, Sloan KB, Flach CR, Mendelsohn R. Imaging the prodrug-to-drug transformation of a 5-fluorouracil derivative in skin by confocal Raman microscopy. J Investig Dermatol. 2007;127(5):1205–9.
20. Zhang G, Flach CR, Mendelsohn R. Tracking the dephosphorylation of resveratrol triphosphate in skin by confocal Raman microscopy. J Control Release. 2007;123(2):141–7.
21. Mendelsohn R, Flach CR, Moore DJ. Determination of molecular conformation and permeation in skin via IR spectroscopy, microscopy, and imaging. Biochim Biophys Acta. 2006;1758(7):923–33.
22. Forster M, Bolzinger M-A, Ach D, Montagnac G, Briancon S. Ingredients tracking of cosmetic formulations in the skin: a confocal Raman microscopy investigation. Pharm Res. 2011;28(4):858–72.
23. Cotte M, Dumas P, Besnard M, Tchoreloff P, Walter P. Synchrotron FT-IR microscopic study of chemical enhancers in transdermal drug delivery: example of fatty acids. J Control Release. 2004;97(2):269–81.
24. Tfayli A, Piot O, Pitre F, Manfait M. Follow-up of drug permeation through excised human skin with confocal Raman microspectroscopy. Eur Biophys J. 2007;36(8):1049–58.
25. Gotter B, Faubel W, Neubert RHH. FTIR microscopy and confocal Raman microscopy for studying lateral drug diffusion from a semisolid formulation. Eur J Pharm Biopharm. 2010;74(1):14–20.
26. Mao G, Flach CR, Mendelsohn R, Walters RM. Imaging the distribution of sodium dodecyl sulfate in skin by confocal Raman and infrared microspectroscopy. Pharm Res. 2012;29(8):2189–201.
27. Crank J. The mathematics of diffusion. London: Oxford University Press; 1975.
28. Saad P, Flach CR, Walters RM, Mendelsohn R. Infrared spectroscopic studies of sodium dodecyl sulphate permeation and interaction with stratum corneum lipids in skin. Int J Cosmet Sci. 2012;34(1):36–43.
29. Oertel RP. Protein conformational changes induced in human stratum corneum by organic sulfoxides: an infrared spectroscopic investigation. Biopolymers. 1977;16(10):2329–45.
30. Zhang G, Moore DJ, Mendelsohn R, Flach CR. Vibrational microspectroscopy and imaging of molecular composition and structure during human corneocyte maturation. J Investig Dermatol. 2006;126(5):1088–94.
31. Almeida PFF, Vaz WLC, Thompson TE. Lateral diffusion in the liquid-phases of dimyristoylphosphatidylcholine cholesterol lipid bilayers-a free-volume analysis. Biochemistry. 1992;31(29):6739–47.
32. Lieb WR, Stein WD. Non-stokesian nature of transverse diffusion within human red-cell membranes. J Membr Biol. 1986;92(2):111–9.
33. Warren PB. Late stage kinetics for various wicking and spreading problems. Cond-mat/0311216v1. 2003.
34. Mack Correa MC, Mao G, Saad P, Flach CR, Mendelsohn R, Walters RM. Molecular interactions of plant oil components with stratum corneum lipids correlate with clinical measures of skin barrier function. Exp Dermatol. 2014;23(1):39–44.
35. Naik A, Pechtold LARM, Potts RO, Guy RH. Mechanism of oleic acid-induced penetration enhancement in vivo in humans. J Control Release. 1995;37(3):299–306.
36. Forslind B. A domain mosaic model of the skin barrier. Acta Derm Venerol. 1994;74(1):1–6.